Chapter 8

SENSORS, ACTUATORS, AND ROBOTS FOR MRI-GUIDED SURGERY AND INTERVENTIONS

Hao Su[*,†], Gang Li[‡], and Gregory S. Fischer[‡]

[*]*Wyss Institute for Biologically Inspired Engineering*
Harvard University, Cambridge, MA, USA
[†]*John A. Paulson School of Engineering and Applied Sciences*
Harvard University, Cambridge, MA, USA
[‡]*Automation and Interventional Medicine (AIM) Robotics Laboratory*
Department of Mechanical Engineering
Worcester Polytechnic Institute, Worcester, MA, USA

With the recent more widespread clinical use of interventional magnetic resonance imaging (MRI), MRI-compatible robotic systems have been heralded as a new approach to assist interventional procedures to allow physicians to treat patients more accurately and effectively. Deploying robotic systems inside MRI synergizes the imaging capability of MRI and the manipulation capability of robotic assistance, formulating the "closed-loop surgery" architecture that utilizes intra-operative imaging to adjust and control the interventional plan. However, MRI imposes unique challenges due to electromagnetic interference, material incompatibility, and confined space inside the MRI bore. This chapter introduces the advantages of MRI-guided surgery and challenges associated with being compatible with the MRI environment. It provides an overview of the state-of-the-art in MRI-compatible sensors, actuators, and robotic systems with future perspectives by discussing the limitations, open questions, and challenges of the current research landscape.

1. Introduction

Ever since the first magnetic resonance imaging (MRI)-guided surgery that was performed for brain tumor resection pioneered by Dr. Ferenc Jolesz[1] at The Brigham and Women's Hospital (affiliate of Harvard Medical School) in 1993, the goal of

MRI-guided surgery is largely the same, that is to perform surgical interventions less invasively, more accurately, more time efficiently, and more effectively.

Typical image-guided surgery (IGS) integrates imaging, registration, spatial tracking, navigation, and interventions. However, often the 3D patient information is pre-operatively acquired with computed tomography (CT) or MRI and registered to the patient during the procedure, and the information used to guide the procedure is essentially "stale" by the time it is used for guidance of the procedure. There is a tremendous need for integrating interactive, real-time, intra-operative imaging into the surgical navigation environment to adjust and control the interventional plan as needed. Deploying robotic systems inside MRI synergizes the imaging capability of MRI and the manipulation capability of robotic surgical assistance. Although the clinical benefits are clear, robot-assisted interventional MRI has thus far failed to become common place due to the challenges associated with utilizing such technology, including in part mechanical constraints of the confined close-bore and electromagnetic compatibility.

1.1. *Motivation of robot-assisted intervention with intra-operative MRI guidance*

The MRI-guided intervention paradigm offers unique advantages over other imaging modalities. MRI provides high-fidelity soft tissue contrast and spatial resolution. Moreover, it is capable of imaging both soft tissue and intervention instruments, thus enabling interactively updated tissue and instrument tracking in MRI. MRI is a multi-parametric imaging modality, and it provides the sensing capability to a variety of physiological parameters, including temperature, strain, blood oxygen level-dependent (BOLD) contrast, etc.[1] MRI produces no ionizing radiation, and thus does not impose the safety hazard to the patient or practitioner of CT or X-ray fluoroscopy.

To improve the intervention outcome of typically manual procedures, deploying robotic systems inside MRI combined the superior imaging capability of MRI with the manipulability of robotic surgical assistance. Potentials for enhanced outcomes include:

(1) **Increase intervention accuracy:** Robotic manipulators can outperform human hands in terms of stability and positioning accuracy thanks to the closed-loop position sensing and control. Further, image-based feedback control enables instrument tracking and motion compensation due to tissue deformation[2] and needle deflection.[3] Hatiboglu *et al.*[4] demonstrated that in over 40% of all cases reported, the surgeons chose to modify their approach based on updated information from intra-operative MRI. Intra-operative updates of the plan

were also observed in MRI-guided urology interventions.[5] Thus, simultaneous imaging and robotic manipulation could facilitate updating and faithfully executing the procedure as planned, even in the presence of unmodeled deformation.

(2) **Reduce procedure time:** As the robot performs the intervention inside the MRI bore, it is often not necessary to repeatedly move the patient out of bore for intervention and back into the bore for imaging confirmation; the procedure duration could potentially be reduced. Further, interleaving live image guidance with in-bore robotic manipulation prevents the need for iterative cycles of imaging and then stopping imaging to enter the room to perform a step of the procedure. In one example, the research group led by Nobuhiko Hata at Brigham and Women's Hospital[6] has demonstrated that a 2-degrees-of-freedom (DOF) robotic system for transperineal prostate biopsy reduced the mean core procedure time in the robotic (90.8 min) than the manual group (100.6 min).

(3) **Reduce cognitive load from surgeon:** As robots can integrate sensors to aid registration, tracking, and navigation, this could reduce the cognitive load of surgeons by minimizing the need to mentally register the images to physical space. A fully integrated system provides an intuitive user interface to plan the procedure, ensures that the surgical plan is referenced to the anatomy of the patient in the scanner, and enables robotic alignment/delivery of the instrument.

(4) **Improve interventional ergonomics:** The ergonomics of manual interventions prove very difficult in the confines of the scanner bore. The diameter of the closed-bore MRI is typically in the range of 60–70 cm, and the distance to reach the isocenter of the MRI bore is in the range of 75–90 cm. These impose an ergonomics burden to manual tool placement procedures, wherein it is difficult to reach into the bore and challenging to accurately perform an intervention in that position. Further, when reaching into the bore, it is difficult to see intra-operative MR imaging, should it be available. Application-specific robots are designed to operate in the constraints of the bore dimensions, while also taking into account the patient positioning and equipment for a given procedure. Further, robots can remain in the bore for a sustained period of time during imaging cycles, and in some cases procedures can be performed via teleoperated control.

1.2. *MRI safety and MRI-compatibility terminologies*

The standard to quantify MRI device safety was defined by the U.S. Food and Drug Administration (FDA), which followed the device classification (ASTM F2503) by the American Society for Testing and Materials (ASTM) as "MR Safe",

Symbol	Term	Definition
	MRI safe	an item that poses no known hazards in all MRI environments. "MR safe" items include non-conducting, non-metallic, non-magnetic items.
	MRI conditional	an item that has been demonstrated to pose no known hazards in a specified MRI environment with specified conditions of use. Field conditions that define the MRI environment include static magnetic field strength, spatial gradient, dB/dt (time varying magnetic fields), RF fields, and specific absorption rate (SAR).
	MRI unsafe	an item that is known to pose hazards in all MRI environments.

Figure 1. ASTM F2503 classification for the MRI devices.

"MR Conditional", and "MR Unsafe" as shown in Fig. 1. A device is considered "MR Safe" if it poses no known hazards in any MRI environments. All these terms are about safety, but neither imaging artifacts nor device functionality is covered. A thorough description of the issues relating to MR safety is described by Shellock.[7]

Bi-directional MRI compatibility means that both the scanner should not disturb the device functionality and the device does not disturb the scanner function (which may cause image artifacts). The MRI scanner may affect the robot in the following ways:

- The static magnetic field can generate torque/force to the device made of ferromagnetic materials (projectile effect).
- Switching gradients and radiofrequency (RF) pulses of the scanner can induce RF interference, leading to electromagnetic interference.
- Moving conducting materials or switching magnetic field gradients could cause eddy currents that may cause thermal, mechanical effects, image distortion, or RF burns in the patient.

Robotic components may also affect MR imaging from both materials and electronics aspects as shown in Fig. 2. With regard to materials, robotic components typically cause susceptibility artifact that is due to variations in the magnetic field strength. Ferromagnetic material causes heavy distortion, and thus should be avoided, while non-ferromagnetic conductors may also induce field distortion.[7] Magnetic field variation causes dephasing of spins and frequency shifts of the surrounding tissues, producing bright and dark areas and spatial distortion. With regard to electronics, electric currents in the devices could induce RF emission signal noise. Typically, stripe and speckle image artifacts (e.g. motor-induced artifact

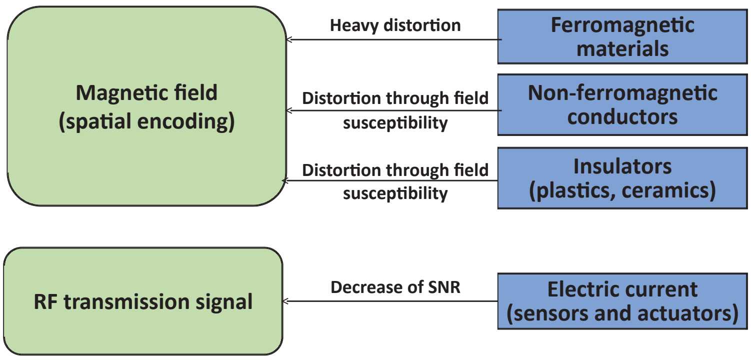

Figure 2. MRI image artifact caused by robotic components.

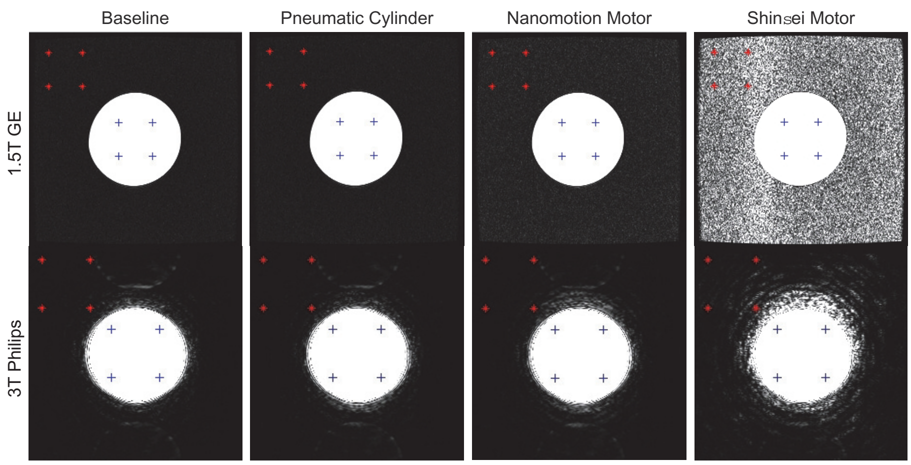

Figure 3. Demonstration of pneumatic and piezoelectric actuations induced image artifact. Representative fast gradient echo (FGRE) images pneumatic motor (pneumatic cylinder) and piezoelectric motors (Nanomotion and Shensei) while moving under both 1.5 and 3 T imaging with 1.5 GE scanner and 3 T Philips scanner. The region of interest (ROI) used in signal-to-noise ratio (SNR) calculations is represented by "+" and the noise ROI is represented by "*".[8]

shown in Fig. 3) are caused by emitted signals. Typical sources of noise include unshielded and unfiltered electrical cables and electronic devices (e.g. switched power supplies or motor actuation signals) that produce rapidly changing currents.

The term "MRI-compatible" is obsolete in terms of the FDA definition; however, it is a commonly used engineering term to describe device functionality and its effect on MRI image quality. Thus, we use this terminology to define its functionality and effect on MR image quality, and MR Safety would be another metric to gauge robot functionality and safety. As summarized in Ref. [9], an "MRI-compatible" device should: (1) not pose any known hazards; (2) not have its intended functions deteriorated by the MRI system; and (3) not significantly affect the quality of the diagnostic information, in the context of a defined application, imaging sequence, and placement within a specific MRI environment.

2. Sensors for MRI-guided Interventions

Sensors are imperative components to enable the "closed-loop surgery" scenario where sensors monitor and provide feedback to the control systems. Sensors are required for both low-level control (e.g. position control) and higher-level control (e.g. tracking and monitoring interactions) of the robot. This section reviews MRI-compatible position sensors and force/torque sensors as they are pervasive and manifest the key sensing principles applicable inside MRI.

2.1. *Position sensors*

Standard methods of position sensing include potentiometers, linear variable differential transformers, capacitive sensors, ultrasonic sensors, magnetic sensors, laser sensors, optical encoders, and cameras (machine vision). Most of these sensing modalities are not readily usable in an MR environment as it might include ferromagnetic materials or electrically active components that could induce image artifact. Besides direct MRI image-based localization, optical encoders have been demonstrated effective in MRI environments.

Standard optical encoders (U.S. Digital, Vancouver, WA, USA) EM1-0-500-I (rotary encoder) and EM1-1-1250-I (linear encoder) with differential line drivers have been thoroughly tested in a 3-T MRI scanner.[10,11] The encoders were incorporated into a pneumatic robot[10] and a piezoelectric robot[11] and performed without any stray or missed counts. The imaging artifact is confined locally to within 2–5 cm from the encoder. This is sufficient because the robots were designed to distance the sensors from the target imaging volume. Other similar optical encoders, both reflective and transmissive, may be effectively used with proper configuration including differential signaling, shielding, and filtering.

Advanced fiber optic encoders (Micronor Inc., CA, USA) are commercially available. This manufacturer's linear position sensor offers 100 μm resolution and 50 μm accuracy. Stoianovici *et al.*[12] developed custom fiber optic quadrature encoders made of plastics for position sensing of a novel pneumatic stepper motor with satisfactory performance.

2.2. *Force sensors*

Force sensing methods inside MRI can be primarily categorized as conventional sensing methods (strain gauge-based methods) and fiber optic force sensing methods. Since strain gauges are the most popular commercially available force sensing method, early force measurement typically utilized this technique. Khanicheh *et al.*[13] developed a hand rehabilitation device incorporating an aluminum strain gauge to investigate brain and motor performance using fMRI. Tse *et al.*[14] designed a biopsy robot using off-the-shelf piezoresistive sensor (First Sensor AG, Germany) to perform bilateral teleoperation in MRI. Kokes *et al.*[15] utilized an industrial force sensor (JR3, California, USA) to perform teleoperated needle insertion.

Due to the underlying electrical property, strain gauges can suffer from electrical noise and tedious installation. These aforementioned sensors can be used in MRI with some distance and safety limitation; thus, fiber optic sensors are one type of promising design alternative for MRI applications due to the magnetically inert property and could potentially thoroughly resolve the compatibility issue.

In terms of the optical modulation mechanism, there are three major types of fiber optic sensors,[16] namely intensity-modulated sensors, wavelength-modulated sensors, and phase-modulated sensors.

2.2.1. *Intensity-modulated fiber optic force sensors*

Intensity-modulated sensors can be categorized as transmissive or reflective sensors. These sensors rely on changes of measured light (usually as a voltage at an optical detector) due to force-induced intensity change. Thus, it possesses the features of simple design, low cost, and easy signal interpretation. Liu *et al.*[17] developed a hydrostatic water pressure transducer to measure hand grip force as shown in Fig. 4(a). But this method has limited accuracy and difficulty to achieve multiple DOF sensing.

The first fiber optic force sensor was proposed by Hirose and Yoneda[18] in 1990 to monitor the relative twist and displacement of flexure in a 6-DOF fiber optic force/torque sensor. This principle is illustrated in Fig. 4(b). Tada *et al.*[19] proposed a 3-DOF transmissive optical micrometry force sensor as shown in Fig. 4(c). Gassert *et al.*[20,21] (Fig. 4(d)) developed reflective fiber optic intensity sensors.

One of the design caveats for an intensity-modulated sensor is the intensity linearity with respect to the sensing distance. As demonstrated by Gassert *et al.*,[22] the response intensity of these optical sensors in function of the distance to the mirror can be divided into two regions: a linear region with high sensitivity and a nonlinear region with decreasing sensitivity as shown in Fig. 5. As a linear response is desired, the distance should be calculated based on the model[24] or experimentally calibrated to ensure that the sensor tip is positioned to be within the linear region of the response curve. Often, these types of sensors also suffer from inaccuracy due to intensity variations as the fiber shape is changed unless a reference channel is used.

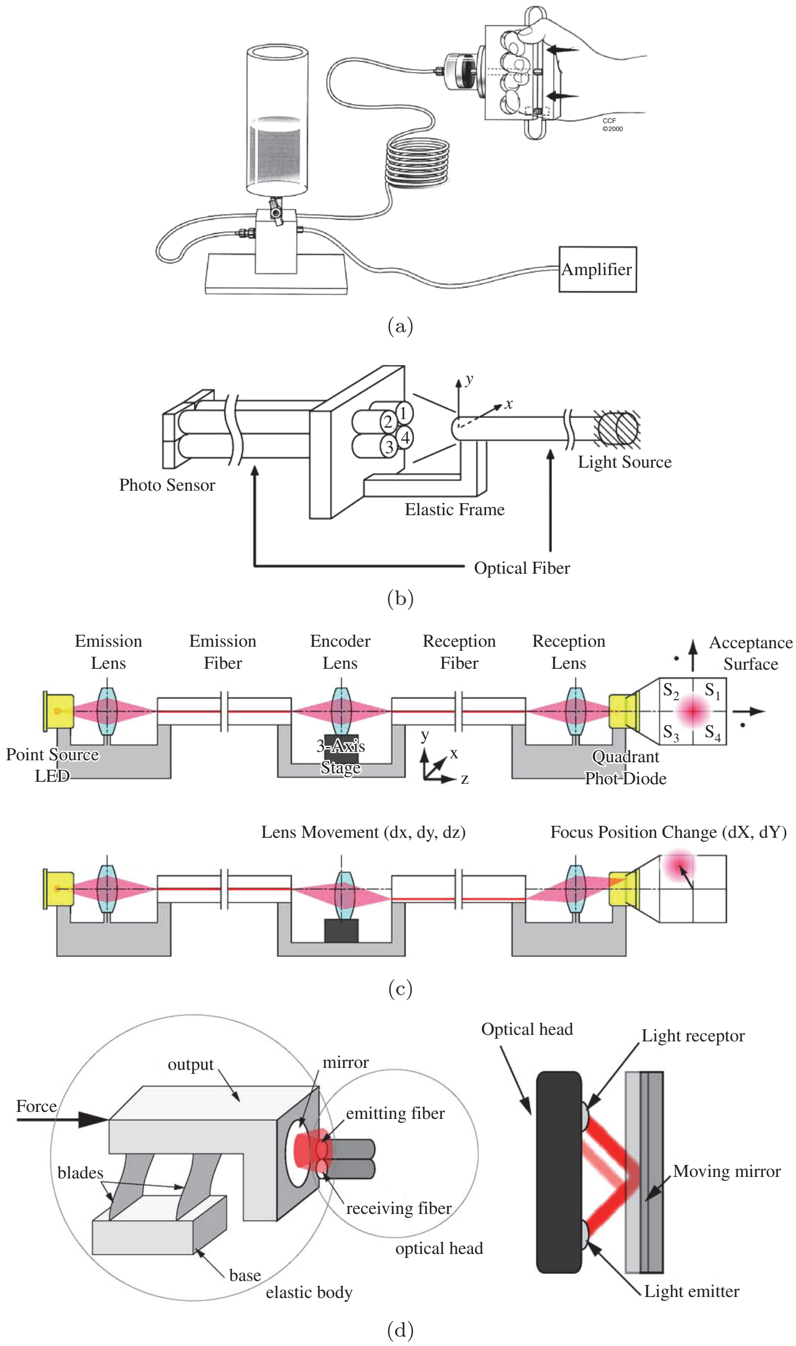

Figure 4. Magnetically inert force sensing principles in MR environments summarized in Ref. [22] © 2008 IEEE. (a) Hydrostatic pressure transducer system for the measurement of hand grip force during fMRI.[17] (b) Differential two-axis optical force sensor for use in an MR environment.[23] (c) Optical micrometry force sensor.[19] (d) Reflected light intensity measurement.[20,21]

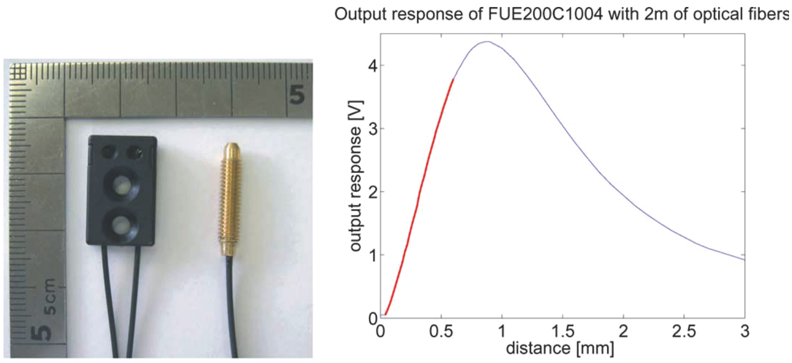

(a) (b)

Figure 5. Fiber optic intensity sensors[22] © 2008 IEEE. (a) Optical heads of a reflected light intensity sensor (FU-38, Keyence, Japan (a)), FUE200C1004 (Baumer Electric, Switzerland (b)). (b) Response of the Baumer sensor with respect to the distance to the reflective surface. The linear region was used for measurement.[22]

2.2.2. *Wavelength-modulated fiber optic force sensor*

To achieve higher sensitivity, wavelength-modulated sensors typically use the fiber Bragg grating (FBG) principle. When an FBG optic cable is interrogated with polychromatic radiation, only a narrow range of wavelengths are reflected. The reflected wavelength shift (Bragg wavelength λ_B) can be expressed[25] as a function of the period of the grating Λ and the effective refractive index η_{eff} as $\lambda_B = 2\Lambda \cdot \eta_{\text{eff}}$. Since Λ and η_{eff} are subjected to temperature and strain, wavelength shift measurement could be used to sense temperature, strain, and physical parameters related to them (e.g. pressure and force).[26]

Endosense SA from Switzerland has developed the TactiCath catheter as shown in Fig. 6(a), an FBG force-sensing ablation catheter to provide physicians with real-time measurement of the contact force between catheter tip and tissue during the catheter ablation procedure. Iordachita *et al.*[27,28] at Johns Hopkins University have developed different versions of FBG sensor with 0.25 μN resolution for retinal microsurgery.

Park *et al.*[25] developed an 18 gauge (1.27 mm) biopsy needle instrumented with 3 FBG sensors for needle bending deflection measurement as shown in Fig. 6(b). Three optical fibers with an outer diameter of 350 μm were bonded in these grooves using a low-viscosity biocompatible cyanoacrylate adhesive. It incorporated temperature compensation algorithm because FBG sensors have high sensitivity to changes in temperature. Though the needle was used for deflection sensing, the underlying principle is applicable for force sensing inside MRI.

Comparing with intensity-modulated sensors, FBG sensors measuring light wavelength are generally less cost-effective as it requires costly optical source and

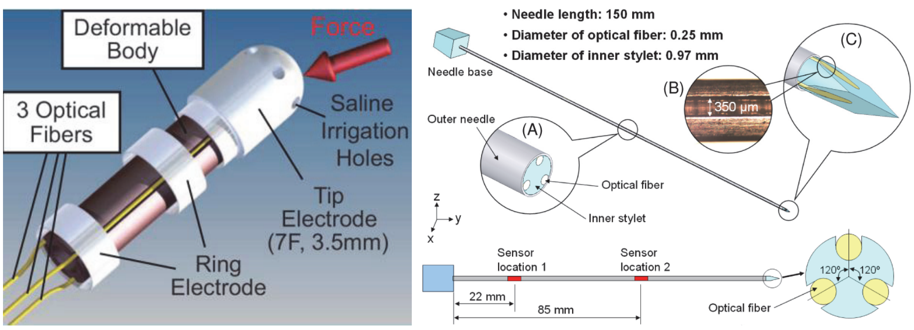

(a) (b)

Figure 6. (a) FBG sensorized catheter TactiCath developed by Endosense SA in collaboration with Stanford University. (b) Instrumented biopsy needle with three FBG optical fibers © 2010 IEEE.

spectral analysis equipment. However, this approach can offer highly stable and accurate sensing in a very compact form factor.

2.2.3. *Phase-modulated fiber optic sensors*

Phase-modulated fiber optic force sensor is based on interferometry that provides displacement and force sensing through the measurement of a relative phase shift between light beams. This sensing principle is shown in Fig. 7(a).[29] Totsu *et al.*[30] developed a miniaturized pressure sensor whose reflective surface (in the form of an aluminum mirror and a conduit) was fabricated with a thin silicon dioxide diaphragm for a 120-μm diameter catheter.

Recently, Su *et al.*[29] and Shang *et al.*[31] designed a fiber optic force sensor based on the Fabry-Perot interferometry (FPI) approach utilizing a commercially available FPI strain gauge (FOS-N-BA-C1-F1-M2-R1-ST, FISO Technologies, Canada) fiber and a custom compact interface unit. This FPI sensor shown in Fig. 7(b), was integrated with a piezoelectrically actuated robot for axial needle insertion force sensing for MRI-guided needle placement.

Besides immunity to electromagnetic and RF signal and substantially lower cost than FBG, the advantages of FPI sensors include: (1) static and dynamic response capability, (2) high sensitivity and resolution, (3) no optical interference due to cable bending, and (4) robust to a large range of temperature variation (-40° to 250°) due to air gap insulation to the sensing region.

3. Actuation Methods for MRI-guided Interventions

Actuator selection is a key design decision for MRI-guided robot development, as material and driver electronics of an actuator are typically the the primary source of

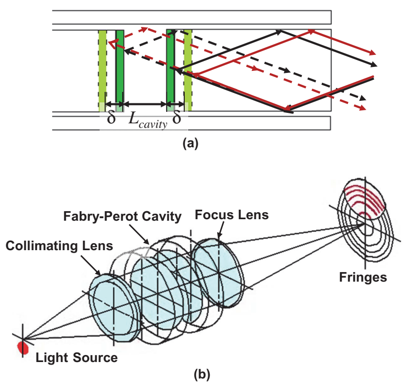

(a)

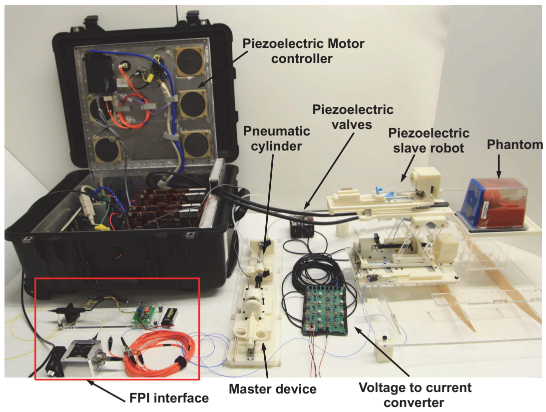

(b)

Figure 7. (a) The working principle of the Fabry-Perot interferometer force sensor[29] © 2011 IEEE. (b) Opto-mechanical implementation of the FPI interface that resides inside the MRI robot controller box[31] © 2013 IEEE.

MRI compatibility issues. Moreover, due to the closed-bore MRI, the constrained space inside the scanner limits the actuator selection, especially for multiple DOF robots whose actuator selection would dominate the dimension of the robotic systems. In general, material, driving electronics, power density, torque density, and compactness are the design considerations for MRI-guided actuation methods. In terms of MR safety and electromagnetic compatibility considerations, actuators for MRI applications can be generally classified into three main categories[32]:

- **Intrinsically MR-Compatible Actuation** which contain no ferromagnetic components and where no electric energy is carried into the MR room. Depending on their placement (distance to the tissue being imaged), non-ferromagnetic conducting materials (i.e. brass, copper, and aluminum) may also be used. This kind of actuation includes hydrostatic actuation, manual actuation, and pneumatic actuation.[32]
- **Electric Actuation** is energetically active, and electrical energy is carried into the MR room either from external power supply or through motors over electric cables inside MR room. Piezoelectric and ultrasonic motors are the mainstream electric actuation used inside MR room.
- **Electromagnetic Actuation** that either take advantage of the high static magnetic field of the MR scanner or contain ferromagnetic components or permanent magnets.[32] To overcome the main safety problem of electromagnetic actuators, Riener *et al.*[33] developed an electromagnetic haptic interface. It was essentially a Lorentz actuator, which contained no ferromagnetic materials and took advantage of the static magnetic field of the scanner. The MRI-powered actuation[34]

pioneered by Dr. Pierre Dupont at Boston Children's Hospital has developed closed-loop commutation control system to interleave pulse sequences for rotor imaging and rotor propulsion.

Manual actuation typically utilizes transmission mechanisms (cable/belt transmission and rod/shaft transmissions and linkages, etc.) to convert manual motion outside of the scanner bore to the robotic motion inside the scanner. Manual actuation has been utilized in robots for breast cancer[35] and cardiac procedures.[36] However, manual actuation suffers from low motion bandwidth. Moreover, it is difficult for multiple DOF motion coordination as the robot would typically be manually controlled in each individual joint space. Hydraulic actuation provides large power output, but cavitation, potential for fluid leakage, and the need to have either a permanently installed closed system or purge hydraulic lines on setup makes it less than ideal for medical applications.[37] Due to its unique advantages for MRI applications, the remainder of this chapter focuses on pneumatic and piezoelectric/ultrasonic actuation methods.

3.1. *Pneumatic actuation*

In terms of image quality and MR-safety, pneumatic actuators can be advantageous over piezoelectric approaches from both material and energetics considerations. The material of pneumatic actuators could be designed not only non-magnetic but also non-conducting, reducing the field inhomogeneity. Disparate from electric actuation that carries electrical energy into the MRI room, pneumatic actuation operates on gas or pressurized air and thus it can fundamentally eliminate electromagnetic interference with the MRI scanner.

A major challenge of pneumatic actuation is accurate position control. Nonlinear friction force and long pneumatic transmission line-induced slow response might cause position overshooting. Fischer *et al.*[10] designed a 4-DOF pneumatic robot and demonstrated 0.94 mm RMS accuracy for a single axis with sliding mode control. Yang *et al.*[38] developed a new sliding mode controller to compensate the long pneumatic transmission line-induced slow response, and its position error at the target is 2.5–5.0 mm.

Since position control is challenging for pneumatic motors, different types of pneumatic stepping motors that do not require precise position regulation have been developed. Figure 8 shows four types of newly developed pneumatic step motors.

Stoianovici *et al.*[39] developed the first pneumatic stepper motor and custom fiber optic incremental encoder. They are made of non-magnetic and dielectric materials such as plastics, ceramics, and rubbers. This motor was utilized in their latest robotic system for transrectal prostate interventions.[40] As shown in Fig. 8(a),

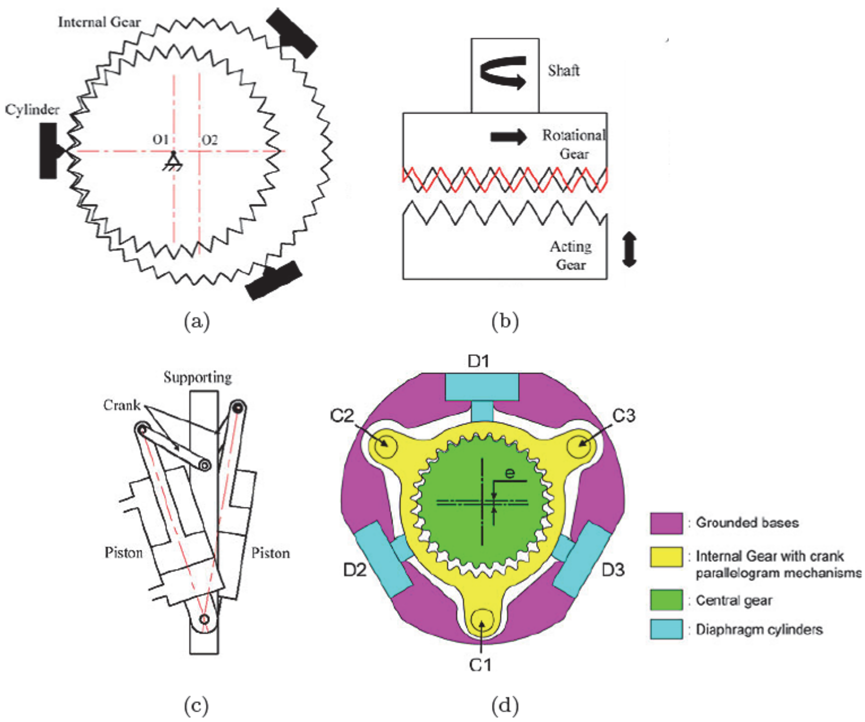

Figure 8. Principles of four types of pneumatic stepper motors[42] © 2016 IEEE. These motors were developed by Stoianovici *et al.*[12] (a), Masamune *et al.*[41] (b), and Chen *et al.*[43] (c). A pneumatic stepper made by additive manufacturing[42] (d). © 2016 IEEE.

it is composed of three diaphragm cylinders, a set of internal gears, and output cranks. It works by sequentially actuating three diaphragm cylinders. The step size of this motor is 3.3° (angular) and 0.06 mm (linear). However, it requires manufacturing numerous components with stringent mechanical tolerance, leading to a high production cost.

Masamune *et al.*[41] proposed a stepper motor that is composed of three pistons within their respective syringes, a rotational gear, and three direct acting gears shown in Fig. 8(b). For each step, the acting gear pushes the rotational gear, then the rotational gear will rotate one stepper to geometrically couple with the acting gear.[42] Sequentially, the motor produces step motion by coordination motion of three acting gears.

Chen *et al.*[43] designed a compact stepper motor based on the principle of automotive engines that have a two-stroke cylinder as shown in Fig. 8(c). The crank transforms the linear motion of the two coupled pistons to rotational motion of the output shaft. The step size of this motor is 3.6° The major advantage is its simplicity and compactness, and its main drawback is the speed discontinuity and vibration.[42]

Wei *et al.*[42] presented a stepper design based on a fan motor as shown in Fig. 8(d). This motor is fabricated with 3D printing and has a requirement on air-tightness. Even though it is not specifically designed for MRI-guided applications, it proposed a promising alternative for motor design that can be rapidly prototyped with a monolithic manufacturing process.

3.2. *Piezoelectric actuations*

Piezoelectric motors are the other mainstream actuation approach for MRI-guided procedures as they operate on the reverse piezoelectric effect without a magnetic field as required by traditional electromagnetic motors. Piezoelectric motors, sometimes referred to as ultrasonic motors depending on the frequency with which they operate, have been utilized for both open MRI[44] and closed-bore MRI.[37] In terms of driving signal, piezoelectric motors fall into two main categories: harmonic and non-harmonic ones. Both have been demonstrated to cause interference within the scanner bore with the commercially available drive systems.[45] Harmonic motors, such as Nanomotion motors (Nanomotion Ltd., Israel), are generally driven with fixed frequency sinusoidal signal on two channels at 38–50 kHz and velocity control is through amplitude modulation of 80–300 V supply. Shinsei harmonic motors (Shinsei Corporation, Japan), however, are speed controlled through frequency modulation with maximum speed at resonance. Figure 9 shows two examples of the Nanomotion and Shinsei motors.

Non-harmonic motors, such as Piezo Legs motors (PiezoMotor AB, Sweden), operate at a lower frequency (750–3000 Hz). Piezo Legs actuators require a

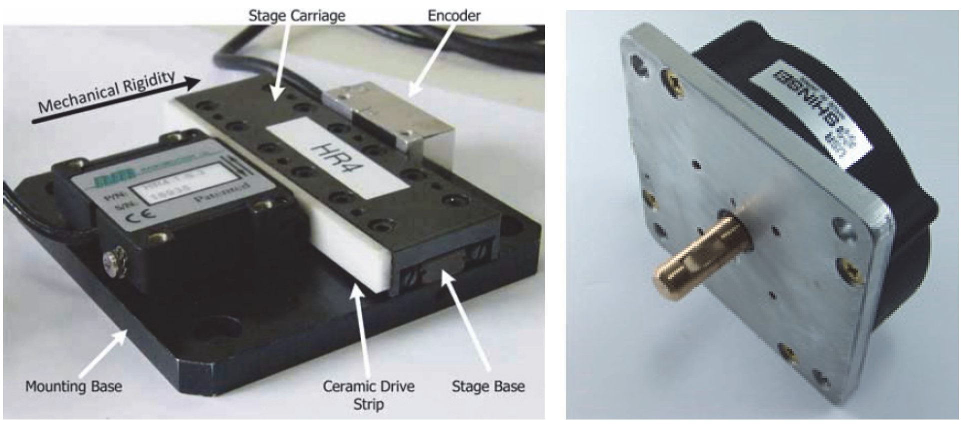

(a) (b)

Figure 9. (a) The legs of the Nanomotion motor (H4, Nanomotion Ltd., Israel) are pre-loaded against the ceramic drive strip and a linear encoder provides closed-loop position feedback. (b) High torque ultrasonic motor example (USR60-S4N, Shinsei Corp., Tokyo, Japan).

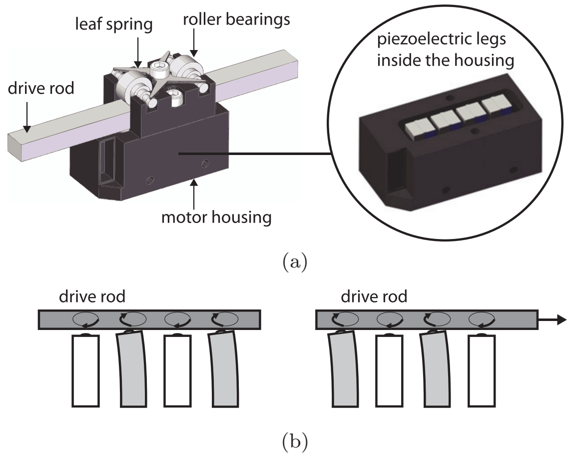

Figure 10. (a) The Piezo Legs motors (PiezoMotor AB, Sweden) are composed of four piezoelectric legs. A ceramic rod is pressed against the legs by two roller bearings and two pre-loaded leaf springs. (b) The drive rod is actuated by friction due to the periodic contact between the legs and rod. Each leg produces an elliptic trajectory during activation. Gray color denotes legs currently in contact with the drive rod.[46] © IOP Publishing 2012.

complex shaped waveform on four channels generated with high precision at fixed amplitude (typically a low voltage of <50V). As shown in Fig. 10, the motor consists of four quasi-static legs (A, B, C, and D legs) forming a stator which interchangeably establishes frictional contact to a ceramic drive pre-loaded with a beryllium copper leaf spring and is operated below their resonant frequency. Each bimorph leg consists of two electrically isolated piezoelectric stacks. The legs elongate when an equal voltage is applied to the two stacks of one leg. Applying different voltages on the two stacks of one leg causes the leg to bend.

Comparing with pneumatics, piezoelectric motors have unparalleled positioning accuracy and power density.[47] For example, the angular resolution of the rotary piezoelectric motor (Piezo Legs, LR80, PiezoMotor AB, Sweden)[11] is $5.73 \times 10^{-6\circ}$ and its dimension is 23 mm diameter by 34.7 mm long. In comparison, the pneumatic stepper motor developed by Stoianovici *et al.*[12] has 3.3° step angle and its dimension is 70 × 20 × 25 mm.

However, piezoelectric motors utilizing commercially available motor drivers have been shown to introduce unacceptable MR imaging noise (up to 40–80% signal loss) during synchronous robot motion.[45] Though there have been efforts to shield motors (such as with RF shielding cloth) and ground the shielded control cables,[45] the MRI compatibly results demonstrate that SNR reduction is up to 80%. From our prior study,[8] the source of noise is primarily from the driving signal rather than the motor itself. Commercially available piezoelectric motor drivers typically use a class-D style amplification system that generates the waveforms by low-pass

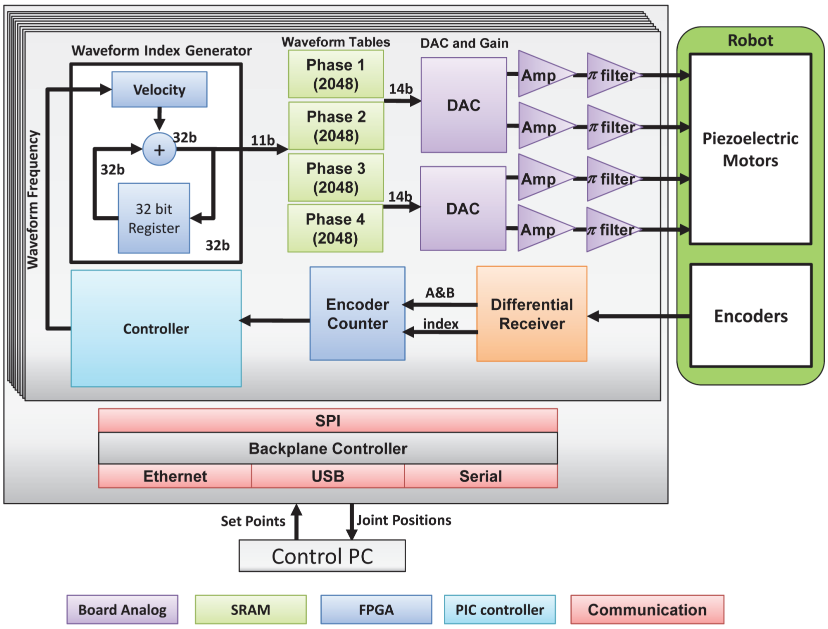

Figure 11. Block diagram of the DDS-based piezoelectric motor driver.[11] An FPGA is configured as a waveform synthesizer generating the four phases of the drive signal which are passed to a linear amplifier stage with integrated filtering. © IEEE 2015.

filtering high-frequency square waves. By using switching drivers (the typical approach since the manufacturers primary design goal was power efficiency instead of noise reduction), significant RF emissions and noise on the motor drive lines are introduced, which can cause interference with imaging. Although filtering can improve the results, it typically has not been effective in eliminating the interference and often significantly degrades motor performance.

Su *et al.*[11] described a piezoelectric motor driver with signals generated from a direct digital synthesizer (DDS), high-performance multi-channel digital-to-analog converter (DAC), high-power linear amplifiers, and π filtered outputs (Figs. 11 and 12). In contrast to commercial drivers based on high-frequency switching voltage regulators, it is capable of cleanly generating both high-voltage sinusoidal signals and low-voltage precise waveforms such that it could be used to drive both harmonic (e.g. Shinsei and Nanomotion) and non-harmonic (e.g. Piezo Legs) commercial available motors.[48]

4. Intra-operative MRI-guided Surgical Robots

This section reviews surgical robotic systems for MRI-guided interventions in terms of surgical procedures, including application-specific examples of robots

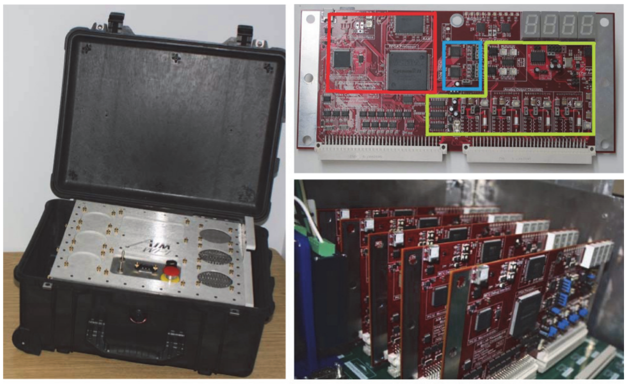

(a) (b)

Figure 12. The prototype of the direct digital synthesizer based piezoelectric motor driver.[11] (a) MRI robot controller enclosed inside a carry on travel case. (b) Piezoelectric motor controller. © IEEE 2015.

for neurosurgery, prostate, and breast interventions; cardiothoracic surgery; and general surgery. Those robotic systems leverage the sensor and actuator innovation in the aforementioned sections, with procedure-specific design features. Due to the previously described constraints, general purpose manipulators are unlikely to be effective broadly for in-bore MRI-guided interventions.

4.1. *MRI-guided neurosurgery robots*

In 1995, Masamune *et al.*[49] at University of Tokyo developed a stereotactic surgery manipulator manufactured with polyethylene terephthalate (PET) linkages and actuated with ultrasonic motors (USR30-N4, Shinsei Corporation, Tokyo, Japan). It was compact enough to fit inside a 0.5 T closed-bore scanner, and was the first of the MRI-compatible robots developed. This robot utilized a remote center of motion (RCM) mechanism with 3-DOF Cartesian motion positioning, 2-DOF angulation (10–60° pitch and $\pm 90^\circ$ yaw), and 1-DOF manual needle insertion.

Since 2007, researchers from the University of Calgary in Canada, led by Dr. Garnette Sutherland, in collaboration with MacDonald, Dettwiler and Associates Ltd. (MDA), have developed the bi-manual general purpose neurosurgery robot NeuroArm[50] to assist surgical procedures inside a 1.5 T intra-operative MRI. NeuroArm, shown in Fig. 13(a), is a master–slave teleoperation system for neurosurgical procedures. The system includes a workstation, a control cabinet, and two slave robot arms mounted on a mobile base. Each slave robot arm has 7-DOF for tool motion control. The two robot arms are placed on a vertically adjustable mobile base. The NeuroArm utilizes 16 ultrasonic motors (HR2-1N-3, Nanomotion Ltd., Israel) controlled with Nanomotion drive electronics. However,

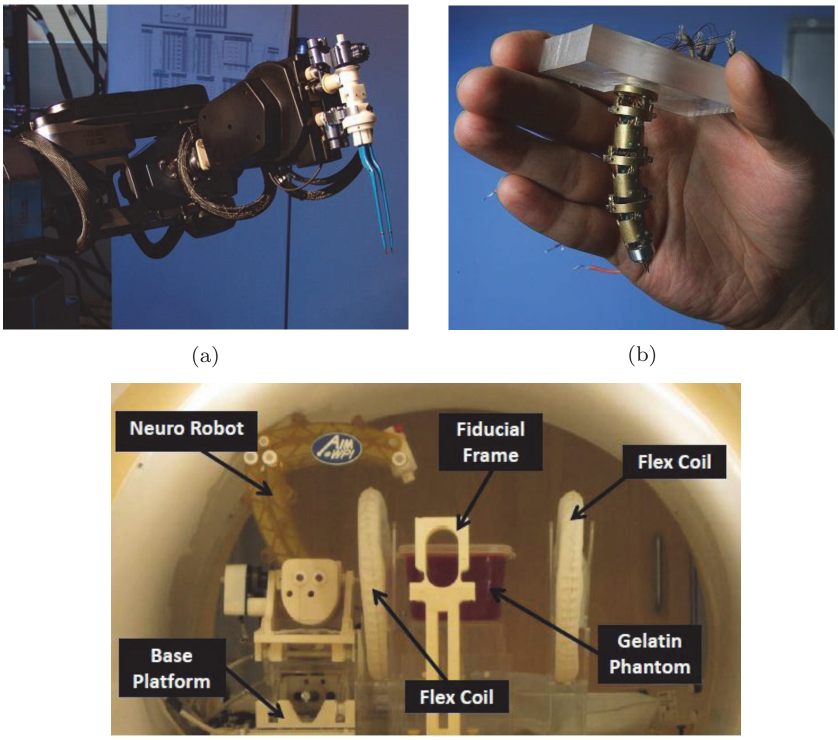

(a) (b)

(c)

Figure 13. MRI-guided neurosurgery robots. (a) NeuroArm robot developed at University of Calgary[50] © 2008 Lippincott Williams and Wilkins. (b) Steerable neurosurgical robot made of hollow brass tubes at University of Maryland[51] © 2010 IEEE. (c) MRI-guided neurosurgical robot developed at Worcester Polytechnic Institute[52] © 2010 Springer.

the motor control electronics has high-frequency driving signal which would cause image artifact during robot motion. Thus, the robot needs to stop motion during imaging, which is a major limitation as it is not able to perform real-time intra-operative manipulation with image guidance. Two haptic devices (Phantom, SensAble Technologies, Inc. USA) are equipped with a stylus that allows 6-DOF position and orientation control over the tool in the manipulator. The arm end-effector is equipped with a fiber optic force sensor for force display to haptic device. This robot has been commercialized by IMRIS Inc. (Deerfield Imaging, USA) for integration with their VISIUS multi-modality surgical theater.

Ho *et al.*[51] from University of Maryland presented an MRI-compatible steerable neurosurgical robot made of hollow brass tubes with 9 mm diameter shown in Fig. 13(b). It is controlled with two antagonistic shape memory alloy (SMA) wires as actuators for each joint. Based on the modeling and characterization of the thermo-mechanical behavior of SMA springs, a pulse width modulation (PWM)-controlled current switching circuit was developed to control the temperature of multiple SMA wires. Low bandwidth, hysteresis, and creep caused position error and high temperature are the limitations of this robot. Comber *et al.*[53] at Vanderbilt University described another type of steerable robot based on the concentric tube mechanism. This pneumatically actuated neurosurgery robot utilized a robust, nonlinear, model-based controller to compensate system nonlinearities achieving 0.03 mm and 0.46° error for the prismatic and revolute joints respectively.

Su *et al.*[54] at Worcester Polytechnic Institute designed a 5-DOF MRI-guided stereotactic system which is kinematically equivalent to a traditional stereotactic Leksell frame. It has a Cartesian positioning stage and pitch and yaw orientation stage. This robot, shown in Fig. 13(c) is actuated by piezoelectric motors (Piezo Legs, PiezoMotor AB, Uppsala, Sweden) and primarily made of polytherimide (PEI, Ultem) and acrylonitrile butadiene styrene (ABS). Besides the manipulator development, a novel ultrasonic ablator tool for Ultrasound Interstitial Thermal Therapy (USITT)[55] is being integrated into the robotic system. With orientation and insertion motion control of this USITT ablator, it has the potential to perform targeted thermal therapy of brain tissue.

4.2. *MRI-guided robots for prostate interventions*

MRI-guided prostate interventional robots have been studied extensively, as reviewed by Tempany and Fichtinger.[1] Transperineal and transrectal interventions are the mainstream interventional methods. Though significantly more invasive than the transrectal and transperineal routes, transgluteal approach was also investigated[56] using the the Innomotion pneumatic MRI-compatible robot (Innomedic GmbH, Philippsburg-Rheinsheim, Germany), which is no longer commercially available. Thus, this section focuses on robots with those two interventional methods.

4.2.1. *Robots for transrectal prostate interventions*

Transrectal access is excellently tolerated by patients as it requires only local anesthesia. Since the current gold standard for prostate biopsy is transrectal ultrasound (TRUS), practitioners usually have extensive prior experience, and so it is easier for workflow adaptation to the MRI-guided transrectal interventions.

Krieger *et al.* at the Johns Hopkins Hospital developed three generations of access to the prostate tissue (APT) robots, starting from a manually controlled manipulator.[57] This robot featured three microtracking coils that are embedded within the device to sense custom-programmed MRI pulse sequences. The

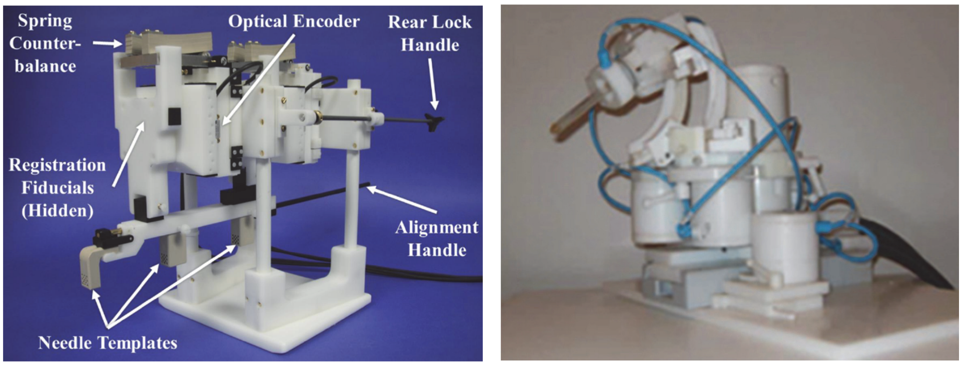

(a) (b)

Figure 14. Transrectal prostate robots. (a) 5-DOF needle guide placement mechanism developed by Cepek *et al.* at Robarts Research Institute, Canada[59] © 2012 Springer and (b) 5-DOF needle guide prostate interventional robot developed by Yakar and Schouten *et al.* at Radboud University Nijmegen Medical Center, Netherlands[60] © 2011 RSNA; © 2010 IEEE.

second-generation APT robot utilized hybrid tracking with gadolinium fiducial and optical encoder,[58] while the third generation[45] incorporated piezoelectric actuation to produce more accurate motion.

Cepek *et al.*[59] at Robarts Research Institute presented a device for delivering prostate focal thermal therapy under MRI guidance shown in Fig. 14(a). Unlike most existing manual devices, this robot is capable of delivering needles to targets in the prostate without removing the patient from the scanner. This feature greatly reduces procedure time and increases accuracy. The manual driven device consists of a mechanical linkage encoded with optical incremental encoders.

Yakar *et al.*[60] from Radboud University Nijmegen Medical Center in the Netherlands described a 5-DOF robotic needle guide manipulator for transrectal prostate biopsies in a 3 T closed-bore MRI scanner (Magnetom Trio, Siemens Medical Solutions, Erlangen, Germany). The robotic manipulator shown in Fig. 14(b), is primarily constructed of plastics. The needle guide has a suction cup working as a safety mechanism, which automatically releases when the force to the patients' rectal wall reaches a preset threshold value.

4.2.2. *Robots for transperineal prostate interventions*

To avoid excessive physical damage to the anterior rectal wall, the transperineal approach is preferred over the transrectal, especially in the case there is a large number of needle insertions.[1] Both piezoelectric and pneumatic actuation have been applied to transperineal interventions.

Utilizing piezoelectric actuation, DiMaio *et al.*[61] at Brigham and Women's Hospital reported a robotic device for needle placement based on the original design

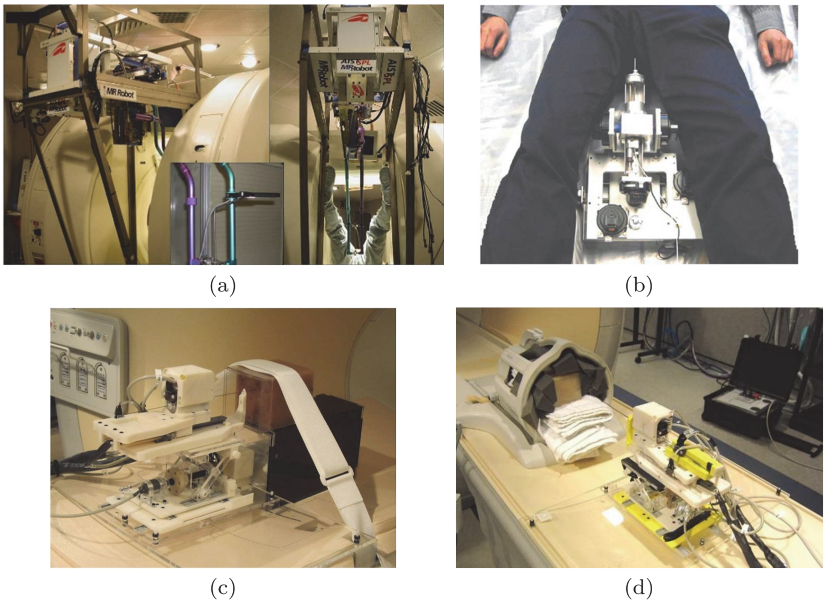

Figure 15. Transperineal prostate robot utilizing piezoelectric actuation. (a) 5-DOF needle guide prostate interventional robot developed by DiMaio *et al.* at Brigham and Women's Hospital[63] © 2007 Informa Plc. (b) 6-DOF needle guide placement robot developed by Goldenberg *et al.* at University of Toronto[37] © 2008 IEEE. (c) 6-DOF needle robot developed by Su *et al.* at Worcester Polytechnic Institute[29] © IEEE 2011. (d) 6-DOF concentric tube continuum robot developed by Su *et al.* at Worcester Polytechnic Institute[64] © IEEE 2012.

by Chinzei[62] that can be used for transperineal prostate biopsy in an open 0.5 Tesla MRI scanner (GE Signa SP, Milwaukee, WI). The ultrasonic motor-driven robot shown in Fig. 15(a) is made of paramagnetic materials, such as titanium alloy and plastics. The robot mechanism is composed of a 2-DOF orientation module and a 3-DOF Cartesian positioning module. Taking advantages of the free space between the two vertical scanner bores (also known as double-donut scanner), the robot was placed on top of the scanner and two long articulated linkages expand down to access the patient. However, this type of open interventional MRI bore has been phasing out and robotic systems for closed-bore MRI are gaining more popularity.

Goldenberg *et al.*[37] designed a 6-DOF prostate interventional robot shown in Fig. 15(b) and aluminum 6061 was the primary material of the robot. A few parts were made of brass and plastic and the needle material was made of titanium.

Su *et al.* developed a 6-DOF straight needle placement robot[11] and a 6-DOF concentric tube continuum robot[64] shown in Figs. 15(c) and 15(d), respectively. Piezoelectric motors (PiezoMotor AB, Uppsala, Sweden) are used for both mechanisms. An upgraded version of this robot[65] has been developed with a novel parallel manipulator using Shinsei motors for increased torque control capability.

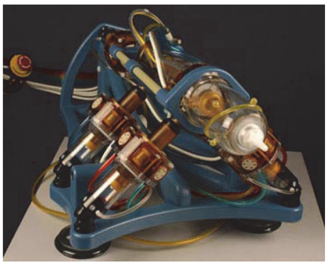

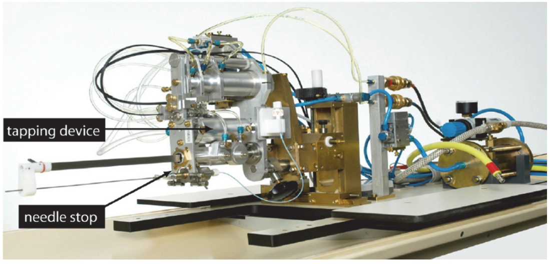

(a) (b)

Figure 16. Transperineal prostate robot utilizing pneumatic actuations. Both robots have actuated needle insertion mechanism. (a) 6-DOF pneumatically actuated robot developed by van den Bosch *et al.* at the University Medical Center Utrecht[67] © 2010 IOP Publishing and (b) 6-DOF pneumatically actuated robot developed by Stoianovici *et al.* at Johns Hopkins University[39] © 2007 Informa Plc.

Utilizing pneumatic actuation, Fischer *et al.* described an MRI-compatible robotic manipulator with four active (X–Y motion and pitch-yaw angulation) and one passive (the encoded needle insertion) DOF.[10]

Two robotic systems that can automatically insert a needle into the patients' prostate under MRI guidance are the one that is built at the University Medical Center Utrecht (UMCU) and the one described by Muntener *et al.*[66] at the Urology Robotics research group led by Dr. Dan Stoianovici at Johns Hopkins University.

van den Bosch *et al.*[67] built the UMCU robot that can be used for transperineal prostate interventions in a closed-bore 1.5 T MRI scanner shown in Fig. 16(a). The robot is made of polymers and non-ferromagnetic materials, such as copper, titanium, and aluminum. It has four passive DOF for needle alignment and one active DOF for needle insertion. The UMCU robot contains a tapping device to tap the needle stepwise toward the prostate. Lagerburg *et al.*[68] demonstrated that needle tapping could reduce tissue deformation in comparison to manual needle insertion.

Muntener *et al.*[66] reported an MRI-compatible robot with 5-DOF (Fig. 16(b)) for transperineal needle interventions of the prostate. This robot is based on the novel pneumatic stepper motor PneuStep.[12] The robot has been tested for MR compatibility in magnetic field strengths up to 7 T.

4.3. *MRI-guided breast surgery robots*

Mammography is the current standard for breast cancer imaging, but it has variable sensitivity especially in dense breast. MRI is sensitive to cancer tissue in the breast and can detect lesions that may be occult on other imaging modalities.[69] Larson *et al.*[35] at University of Minnesota designed a system (Fig. 17) for breast biopsy with MRI guidance. It stabilizes the breast with compression. To avoid image

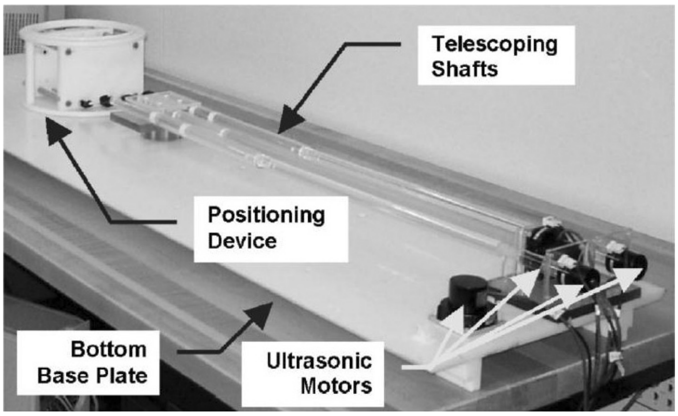

Figure 17. MRI-guided breast biopsy robot at the University of Minnesota uses telescopic rods to actuate movement while keeping the ultrasonic motor away from imaging bore[35] © 2004 ASME.

artifact due to the ultrasonic motors, five telescopic rods were used to remotely actuate probes. Due to remote actuation, the mechanism took about 50 s to place a probe with sub-millimeter repeatability. Moreover, when the target was more than 40 mm away from the rotation axis of the device, backlash in the rotating joints could induce up to 5 mm of error at the tip.

Yang *et al.*[70] presented a pneumatically/piezoelectrically hybrid actuated parallel robot. It includes an X–Y stage (2 linear DOF) with piezoelectric actuation, a 3-DOF parallel mechanism (2 rotation DOF and 1 translation DOF), and one needle driver (1 linear DOF). Since the piezoelectric motors (Nanomotion Ltd., Israel) using commercial motor drivers would cause image artifact, the needle driver insertion utilized a telescopically actuated lead screw mechanism with piezoelectric motors shown in Fig. 18.

In 2016, Chan *et al.*[69] at the McMaster University, Canada developed the Image-guided Automated Robot (IGAR) for breast biopsy. In a phantom model, it demonstrated an accuracy of 0.34 mm and a repeatability of 0.2 mm. In a clinical human trial, it achieved a clinical degree of accuracy in an end-to-end procedure.

4.4. *MRI-guided cardiothoracic surgery robots*

Li *et al.*[71] at National Institutes of Health (NIH) developed a pneumatically actuated robotic assistant system for transapical aortic valve replacement under MRI guidance in a beating heart shown in Fig. 19.

An Innomotion robot (Innomedic GmbH) with custom developed hands-on cooperative interface was used as a device holder. A compact 2-DOF pneumatically actuated delivery module was developed for controlling both balloon-expandable and self-expanding prostheses. This pneumatic cylinder was based upon the ones

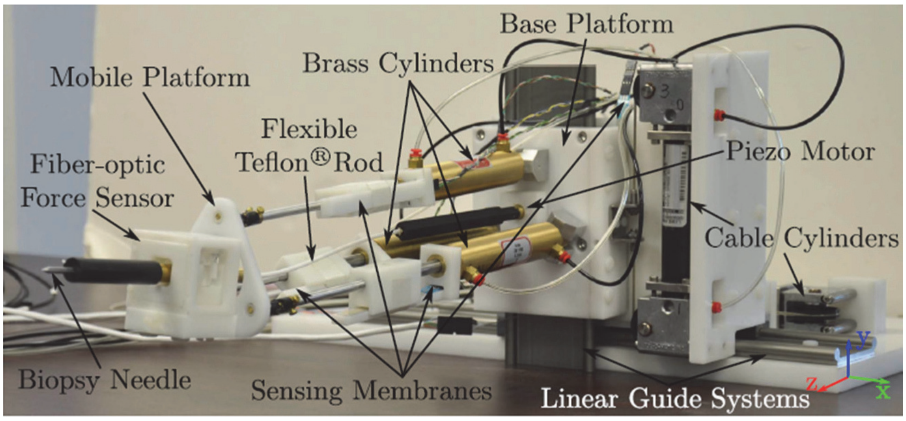

Figure 18. Parallel robot developed at University of Maryland for breast biopsy actuated by piezoelectric motors for $X-Y$ stage motion and pneumatic actuation for parallel mechanism motion (2 rotation DOF and 1 translation DOF)[70] © 2011 IEEE.

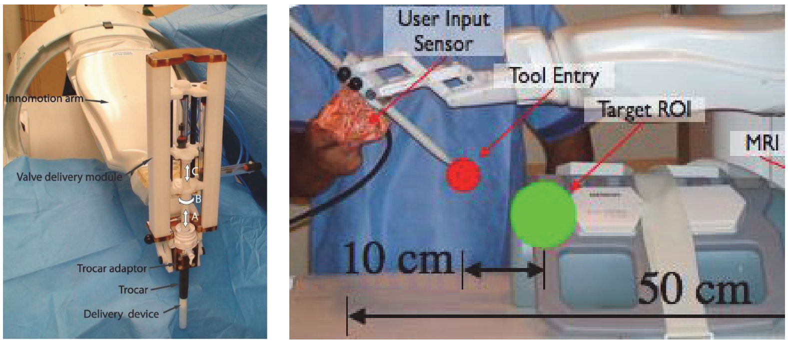

(a) (b)

Figure 19. Pneumatic actuated robotic assistant for aortic valve replacement under MRI guidance developed at National Institutes of Health. This system was adapted from the Innomotion arm with a 2-DOF robotic delivery module.[71] (a) Robot setup with Innomotion robot and image guided delivery module. (b) Robot setup with Innomotion robot and "user input sensor" © 2011 IEEE.

developed by Fischer *et al.*[10] A compact fiducial that requires a single imaging slice was used for image-based robot registration.

Zemiti *et al.*[72] in France developed a light puncture robot (LPR) with patient mount to perform puncture interventions, compatible with both CT and MRI shown in Fig. 20(a). The LPR has 5-DOF including a 3-DOF needle holder and 2-DOF translational motion platform. The needle holder provides needle axis translation, roll rotation motion, and pitch rotation motion.

Wu *et al.*[73] described the design of a 2-DOF (pitch and yaw) guidance device for faster and more accurate alignment and insertion of multiple probes

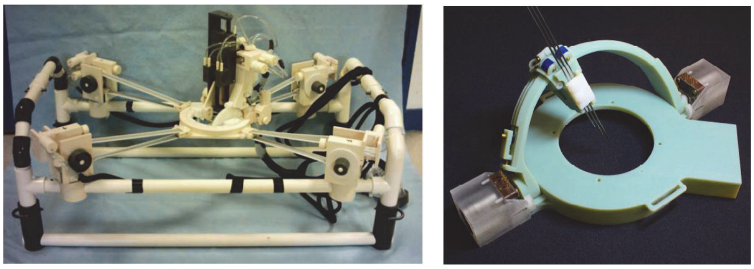

(a) (b)

Figure 20. MRI-guided robot for cardiothoracic surgery with patient mount. (a) LPR system with pneumatic actuation developed in Grenoble, France[72] © IEEE 2008. (b) 2-DOF MRI coil mounted multi-probe robotic positioner[73] © ASME 2013.

during cryoablation and other percutaneous interventions performed in closed-bore MRI. The 3D printed prototype shown in Fig. 20(b) positions multiple probes for MRI-guided percutaneous interventions. This mechanism offers a practical and cost-effective approach for the placement of multiple ablation probes. The robot was integrated to an MRI coil, and is thus compact, portable, and easy for surgical workflow development. In 2014, Salimi *et al.*[74] University of Houston, developed a 4-DOF patient-mounted and cable-driven manipulator to assist beating heart intra-cardiac interventions.

4.5. *MRI-guided general surgery and abdominal intervention robots*

One general purpose MRI-compatible interventional system was recently developed by Tsekos *et al.* and further improved by Christoforou *et al.*[36] The device has 7-DOF and consists of a Cartesian positioner with three orthogonal DOF (3-DOF for *XYZ* motion) located in front of the MR scanner and a robotic arm that was deployed inside the scanner. The arm has 3-DOF for orientation control and a linear DOF for the insertion of interventional tools.

Hashizume *et al.*[75] in Japan developed an MRI-guided surgical robotic system for minimally invasive surgery. This robotic system is novel in the sense that it combines laparoscopic imaging with MRI, enabling visualization of both exterior and interior tissues. The system consists of an MRI guidance module, an MRI-compatible operating table module, and an MRI-compatible master–slave surgical manipulator module. The MRI image guidance module, depicted in Fig. 21, includes pre-operative planning, an interactive scan control (ISC) imaging, and 3D navigation.

In 2016, Franco *et al.*[76] described an MRI-guided robot for laser ablation of liver tumors. Robot-assisted procedures were successfully completed on two

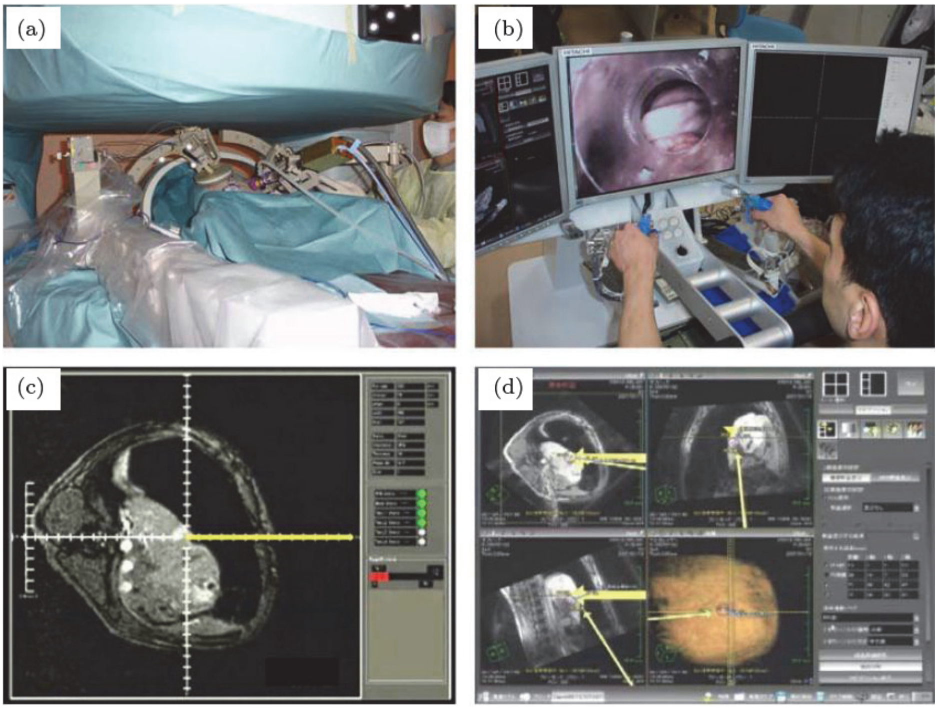

Figure 21. MRI-compatible master/slave system and human–machine interface. (a) Slave surgical manipulator inside open MRI scanner. (b) Bimanual master manipulator. (c) Interactive scan control image interface. (d) 3D navigation software[75] © 2008 Springer.

patients.[77] The pilot study endorsed the clinical use of the robot as it was fully functional and was suitable for double-oblique needle insertions.

5. Discussion and Conclusion

This chapter reviewed sensors, actuators, and robotic systems for MRI-guided surgical interventions. Significant effort has been spent to address fundamental sensing and actuation issues to maintain MR safety and image quality. Even though with the advancement of MRI-guided robotics, most of the systems are in preliminary prototype phase, it is desirable to evaluate its functionality, effectiveness in terms of operational duration and targeting accuracy, and workflow integration.

Most animal and human clinical trials are for prostate interventions,[40,60,78] potentially because most early robotic systems were developed for prostate interventions. The interventional robot[65] has gone through human clinical trials for prostate biopsy of 11 patients at the Brigham and Women's Hospital. All 11 procedures were successfully performed in 102.624.5 min with targeting errors of 4.92.9 mm. Preliminary results have shown its feasibility and clinical potential.

Hata *et al.*[6] has shown that robotic assistance not only reduces the procedure time but also enhances the targeting accuracy in comparison to the manual approach. But cancer yields and complication rates were not statistically different between the robot-assisted and manual intervention groups.

More and more MRI-guided robotic systems are going through human clinical trials ranging from liver ablation[77] to breast biopsies.[69] Besides the demonstration of robot safety and functionality, robotic assistance has shown advantages and potential in terms of accuracy and procedure duration. It is crucial to define clinical metrics, such as improved cancer detection yield, to systematically evaluate the efficacy beyond these aspects.

References

1. Jolesz, F. (2014). *Intraoperative Imaging and Image-Guided Therapy* (Springer Science and Business Media).
2. Patel, N. A., van Katwijk, T., Li, G., Moreira, P., Shang, W., Misra, S. and Fischer, G. S. (2015). Closed-loop asymmetric-tip needle steering under continuous intraoperative MRI guidance. In *Annual Int. Conf. IEEE Engineering in Medicine and Biology Society, EMBC*, pp. 6687–6690.
3. Tadayyon, H., Lasso, A., Kaushal, A., Guion, P. and Fichtinger, G. (2011). Target motion tracking in MRI-guided transrectal robotic prostate biopsy. *IEEE Trans. Biomed. Eng.*, 58(11), 3135–3142.
4. Hatiboglu, M., Weinberg, J. and Suki, D. (2009). Impact of intraoperative high-field magnetic resonance imaging guidance on glioma surgery: A prospective volumetric analysis. *Neurosurgery*, 64(6), 1073–1081.
5. Fennessy, F. M., Tuncali, K., Morrison, P. R. and Tempany, C. M. (2008). MR imaging-guided interventions in the genitourinary tract: An evolving concept. *Radiol. Clin. North Am.*, 46(1), 149–166.
6. Tilak, G., Tuncali, K., Song, S.-E., Tokuda, J., Olubiyi, O., Fennessy, F., Fedorov, A., Penzkofer, T., Tempany, C. and Hata, N. (2015). 3T MR-guided in-bore transperineal prostate biopsy: A comparison of robotic and manual needle-guidance templates. *J. Magnet. Reson. Imag.*, 42(1), 63–71.
7. Shellock, F. G. (2002). Magnetic resonance safety update 2002: implants and devices. *J. Magn. Reson. Imag.*, 16(5), 485–496.
8. Fischer, G. S., Krieger, A., Iordachita, I., Csoma, C., Whitcomb, L. L. and Fichtinger, G. (2008). MRI compatibility of robot actuation techniques — A comparative study. *Int. Conf. Med. Image Comput. Comput. Assist. Interv.*, 509–517.
9. Yu, N., Murr, W., Blickenstorfer, A., Kollias, S. and Riener, R. (2007). An fMRI compatible haptic interface with pneumatic actuation. *2007 IEEE 10th Int. Con. Rehabilitation Robotics*, IEEE, Piscataway, NJ, USA, pp. 714–20.
10. Fischer, G. S., Iordachita, I., Csoma, C., Tokuda, J., DiMaio, S. P., Tempany, C. M., Hata, N. and Fichtinger, G. (2008). MRI-compatible pneumatic robot for transperineal prostate needle placement. *IEEE/ASME Trans. Mechatron.*, 13(3), 295–305.
11. Su, H., Shang, W., Cole, G., Li, G., Harrington, K., Camilo, A., Tokuda, J., C. M. Tempany, Hata, N. and Fischer, G. S. (2015). Piezoelectrically-actuated robotic system for MRI-guided prostate percutaneous therapy. *IEEE/ASME Trans. Mechatron.*, 99(3), 1–13.
12. Stoianovici, D., Patriciu, A., Petrisor, D., Mazilu, D. and Kavoussi, L. (2007). A new type of motor: Pneumatic step motor. *IEEE/ASME Trans. Mechatron.*, 12(1), 98–106.

13. Khanicheh, A., Muto, A., Triantafyllou, C., Weinberg, B., Astrakas, L., Tzika, A. and Mavroidis, C. (2005). MR compatible ERF driven hand rehabilitation device. In *9th Int. Conf. Rehabilitation Robotics, 2005. ICORR 2005*, pp. 7–12.
14. Tse, Z., Elhawary, H., Rea, M., Young, I., Davis, B. and Lamperth, M. (2009). A haptic unit designed for magnetic-resonance-guided biopsy. *Proc. Instit. Mech. Eng., Part H (J. Eng. Med.)*, 223(H2), 159–72.
15. Kokes, R., Lister, K., Gullapalli, R., Zhang, B., MacMillan, A., Richard, H. and Desai, J. P. (2009). Towards a teleoperated needle driver robot with haptic feedback for RFA of breast tumors under continuous MRI. *Med. Image Anal.*, 13(3), 445–455.
16. Polygerinos, P., Zbyszewski, D., Schaeffter, T., Razavi, R., Seneviratne, L. and Althoefer, K. (2010). MRI-compatible fiber-optic force sensors for catheterization procedures. *IEEE Sensors J.*, 10(10), 1598–1608.
17. Liu, J. Z., Luduan, Z., Brown, R. W. and Yue, G. H. (2004). Reproducibility of fMRI at 1.5 T in a strictly controlled motor task. *Magnet. Reson. Med.*, 52(4), 751–60.
18. Hirose, S. and Yoneda, K. (1990). Development of optical six-axial force sensor and its signal calibration considering nonlinear interference. In *1990 IEEE Int. Conf. 1990 Proc. Robotics and Automation*, Vol. 1, pp. 46–53.
19. Tada, M. and Kanade, T. (2005). Design of an MR-compatible three-axis force sensor. In *Proc. IEEE/RSJ Int. Conf. Intelligent Robots and Systems (IROS 2005)*, pp. 3505–3510.
20. Chapuis, D., Gassert, R., Sache, L., Burdet, E. and Bleuler, H. (2004). Design of a simple mri/fmri compatible force/torque sensor. In *Proc. 2004 IEEE/RSJ Int. Conf. Intelligent Robots and Systems, 2004 (IROS 2004)*, Vol. 3, pp. 2593–2599.
21. Gassert, R., Dovat, L., Lambercy, O., Ruffieux, Y., Chapuis, D., Ganesh, G., Burdet, E. and Bleuler H. (2006). A 2-dof fMRI compatible haptic interface to investigate the neural control of arm movements. In *Proc. 2006 Conf. Int. Robotics and Automation*, Piscataway, NJ, USA, pp. 3825–31.
22. Gassert, R., Chapuis, D., Bleuler, H. and Burdet, E. (2008). Sensors for applications in magnetic resonance environments. *IEEE/ASME Trans. Mechtron.*, 13(3), 335–344.
23. Takahashi, N., Tada, M., Ueda, J., Matsumoto, Y. and Ogasawara, T. (2003). An optical 6-axis force sensor for brain function analysis using fMRI. Vol. 1, *Proceedings of IEEE Sensors 2003 (IEEE Cat. No.03CH37498)*, Piscataway, NJ, USA, pp. 253–258.
24. Puangmali, P., Althoefer, K. and Seneviratne, L. (2010). Mathematical modeling of intensity-modulated bent-tip optical fiber displacement sensors. *IEEE Trans. Instrument. Measurement*, 59(2), 283 –291.
25. Park, Y.-L., Elayaperumal, S., Daniel, B., Ryu, S. C., Shin, M., Savall, J., Black, R., Moslehi, B. and Cutkosky, M. (2010). Real-time estimation of 3-D needle shape and deflection for MRI-guided interventions, *IEEE/ASME Trans. Mechatron.*, 15(6), 906–915.
26. Taffoni, F., Formica, D., Saccomandi, P., Pino, G. D. and Schena, E. (2013). Optical fiber-based MR-compatible sensors for medical applications: an overview. *Sensors*, 13(10), 14105–14120.
27. He, X., Balicki, M. A., Kang J. U., Gehlbach P. L., Handa J. T., Taylor R. H. and Iordachita I. I. (2012). Force sensing micro-forceps with integrated fiber bragg grating for vitreoretinal surgery. In *SPIE BiOS*, International Society for Optics and Photonics, 82180W.
28. Liu, X., Iordachita, I. I., He, X., Taylor, R. H. and Kang, J. U. (2012). Miniature fiber-optic force sensor based on low-coherence fabry-perot interferometry for vitreoretinal microsurgery. *Biomed. Opt. Exp.*, 3(5), 1062–1076.
29. Su, H., Zervas, M., Cole, G., Furlong, C. and Fischer, G. S. (2011). Real-time MRI-guided needle placement robot with integrated fiber optic force sensing. *IEEE ICRA Int. Conf. Robotics and Automation*.
30. Totsu, K., Haga, Y. and Esashi, M. (2004). Ultra-miniature fiber-optic pressure sensor using white light interferometry. *J. Micromech. Microeng.*, 15(1), 71.

31. Shang, W., Su, H., Li, G. and Fischer, G. (2013). Teleoperation system with hybrid pneumatic-piezoelectric actuation for MRI-guided needle insertion with haptic feedback. In *IEEE/RSJ Int. Conf. Intelligent Robots and Systems*.
32. Gassert, R., Yamamoto, A., Chapuis, D., Dovat, L., Bleuler, H. and Burdet, E. (2006). Actuation methods for applications in MR environments. *Concepts Magnet. Reson. Part B: Magnet. Reson. Eng.*, 29B(4), 191–209.
33. Riener, R., Villgrattner, T., Kleiser, R., Nef, T. and Kollias, S. (2006). fMRI-compatible electromagnetic haptic interface. In *2005 IEEE Engineering in Medicine and Biology 27th Annual Conference*, IEEE, pp. 7024–7027.
34. Felfoul, O., Becker, A., Bergeles, C. and Dupont, P. E., (2015). Achieving commutation control of an mri-powered robot actuator. *IEEE Trans. Robotics*, 31(2), 387–399.
35. Larson, B. T., Erdman, A. G., Tsekos, N. V., Yacoub, E., Tsekos, P. V. and Koutlas, I. G. (2004). Design of an MRI-compatible robotic stereotactic device for minimally invasive interventions in the breast. *J. Biomech. Eng.*, 126(4), 458–465.
36. Tsekos, N., Khanicheh, A., Christoforou, E. and Mavroidis, C. (2007). Magnetic resonance-compatible robotic and mechatronics systems for image-guided interventions and rehabilitation: A review study. *Annu. Rev. Biomed. Eng.*, 9, 351–387.
37. Goldenberg, A., Trachtenberg, J., Kucharczyk, W., Yi, Y., Haider, M., Ma, L., Weersink, R. and Raoufi, C. (2008). Robotic system for closed-bore MRI-guided prostatic interventions. *IEEE/ASME Trans. Mechatron.*, 13(3), 374–379.
38. Yang, B., Tan, U.-X., McMillan, A. B., Gullapalli, R. and Desai, J. P. (2011). Design and control of a 1-DOF MRI-compatible pneumatically actuated robot with long transmission lines. *IEEE/ASME Trans. Mechatron.*, 16(6), 1040–1048.
39. Stoianovici, D., Song, D., Petrisor, D., Ursu, D., Mazilu, D., Muntener, M., Mutener, M., Schar, M. and Patriciu, A. (2007). MRI Stealth robot for prostate interventions. *Minim. Invasive Ther. Allied Technol.*, 16(4), 241–248.
40. Stoianovici, D., Kim, C., Srimathveeravalli, G., Sebrecht, P., Petrisor, D., Coleman, J., Solomon S. B. and Hricak, H. (2014). MRI-safe robot for endorectal prostate biopsy. *IEEE/ASME Trans. Mechatron.*, (99), 1–11.
41. Sajima, H., Kamiuchi, H., Kuwana, K., Dohi, T. and Masamune, K. (2012). MR-safe pneumatic rotation stepping actuator. *J. Robot. Mechatron.*, 24(5), 820–827.
42. Wei, Y., Chen, Y., Yang, Y. and Li, Y. (2016). Novel design and 3d printing of non-assembly controllable pneumatic robots. *IEEE/ASME Trans. Mechatron.*, 10, 906–915.
43. Chen, Y., Kwok, K.-W. and Tse, Z. T. H. (2014). An MR-conditional high-torque pneumatic stepper motor for MRI-guided and robot-assisted intervention. *Ann. Biomed. Eng.*, 42(9), 1823–1833.
44. Sato, I., Nakamura, R. and Masamune, K. (2010). MRI compatible manipulator with MRI-guided needle insertion support system. In *2010 Int. Symp. Micro-NanoMechatronics and Human Science (MHS)*, pp. 77 –82.
45. Krieger, A., Song, S., Bongjoon Cho, N., Iordachita, I., Guion, P., Fichtinger, G. and Whitcomb L. L. (2012). Development and evaluation of an actuated MRI-compatible robotic system for MRI-guided prostate intervention. *IEEE/ASME Trans. Mechatron.*, (99), 1–12.
46. Szufnarowski, F. and Schneider, A. (2012). Two-dimensional dynamics of a quasi-static legged piezoelectric actuator. *Smart Mater. Struct.*, 21(5), 055007.
47. Huber, J., Fleck, N. and Ashby, M. (1997). The selection of mechanical actuators based on performance indices. *Proc. Roy. Soc. London. Series A: Math. Phys. Eng. Sci.*, 453(1965), 2185–2205.
48. Fischer, G. S., Cole, G. A. and Su, H. (2011). Approaches to creating and controlling motion in MRI. In *Ann. Int. Conf. IEEE Engineering in Medicine and Biology Society, EMBC*, pp. 6687–6690.

49. Masamune, K., Kobayashi, E., Masutani, Y., Suzuki, M., Dohi, T., Iseki, H. and Takakura, K. (1995). Development of an MRI-compatible needle insertion manipulator for stereotactic neurosurgery. *J. Image Guided Surg.*, 1(4), 242–248.
50. Sutherland, G. R., Latour, I., Greer, A. D., Fielding, T., Feil, G. and Newhook, P. (2008). An image-guided magnetic resonance-compatible surgical robot. *Neurosurgery*, 62(2), 286–92; discussion 292–3.
51. Ho, M., McMillan, A., Simard, J., Gullapalli, R. and Desai, J. (2012). Toward a SMA-actuated MRI-compatible neurosurgical robot. *IEEE Trans. Robot.*, 28(1), 213–222.
52. Cole, G., Harrington, K., Su, H., Camilo, A., Pilitsis, J. and Fischer, G. (2010). Closed-loop actuated surgical system utilizing real-time *in-situ* MRI guidance. In *12th Int. Symp. Experimental Robotics — ISER 2010*, New Delhi and Agra, India.
53. Comber, D. B., Barth, E. J. and Webster, R. J. (2014). Design and control of an magnetic resonance compatible precision pneumatic active cannula robot. *J. Med. Dev.*, 8(1), 011003.
54. Li, G., Su, H., Cole, G., Shang, W., Harrington, K., Camilo, A., Pilitsis, J. G. and Fischer, G. S. (2015). Robotic system for MRI-guided stereotactic neurosurgery. *IEEE Trans. Biomed. Eng.*, 62(4), 1077–1088.
55. Nau Jr, W. H., Diederich, C. J., Simko, J., Juang, T., Jacoby, A. and Burdette, E. C. (2007). Ultrasound interstitial thermal therapy (USITT) for the treatment of uterine myomas. In *Biomedical Optics (BiOS) 2007*, International Society for Optics and Photonics, pp. 64400F–64400F.
56. Zangos, S., Herzog, C., Eichler, K., Hammerstingl, R., Lukoschek, A., Guthmann, S., Gutmann, B., Schoepf, U. J., Costello, P. and Vogl, T. J. (2007). MR-compatible assistance system for punction in a high-field system: device and feasibility of transgluteal biopsies of the prostate gland. *Eur. Radiol.*, 17(4), 1118–1124.
57. Krieger, A., Susil, R. C., Menard, C., Coleman, J. A., Fichtinger, G., Atalar, E. and Whitcomb L. L. (2005). Design of a novel MRI compatible manipulator for image guided prostate interventions. *IEEE Trans. Biomed. Eng.*, 52(2), 306–313.
58. Krieger, A., Iordachita, I. I., Guion, P., Singh, A. K., Kaushal, A., Ménard, C. Pinto, P. A., Camphausen, K., Fichtinger, G. and Whitcomb, L. L. (2011). An MRI-compatible robotic system with hybrid tracking for MRI-guided prostate intervention. *IEEE Trans. Biomed. Eng.*, 58(11), 3049–3060.
59. Cepek, J., Chronik, B., Lindner, U., Trachtenberg, J. and Fenster, A. (2012). Development of an MRI-compatible device for prostate focal therapy. In *Medical Image Computing and Computer-Assisted Intervention — MICCAI 2012*, Springer, pp. 455–462.
60. Yakar, D., Schouten, M. G., Bosboom, D. G. H., Barentsz, J. O., Scheenen, T. W. J. and Futterer J. J. (2011). Feasibility of a pneumatically actuated MR-compatible robot for transrectal prostate biopsy guidance. *Radiology*, 260(1), 241–247.
61. DiMaio, S. P., Pieper, S., Chinzei, K., Hata, N., Haker, S. J., Kacher, D. F., Fichtinger, G., Tempany, C. M. and Kikinis, R. (2007). Robot-assisted needle placement in open MRI: system architecture, integration and validation. *Comput. Aided Surgery*, 12(1), 15–24.
62. Chinzei, K., Warfield, S. K., Hata, N., Tempany, C. M. C., Jolesz, F. A. and Kikinis, R. (Mar 2003). Planning, simulation and assistance with intraoperative mri. *Minim. Invasive. Ther. Allied Technol.*, 12(1), 59–64.
63. DiMaio, S., Pieper, S., Chinzei, K., Hata, N., Haker, S., Kacher, D., Fichtinger, G., Tempany, C. and Kikinis, R. (2007). Robot-assisted needle placement in open MRI: System architecture, integration and validation. *Comput. Aided Surgery*, 12(1), 15–24.
64. Su, H., Cardona, D., Shang, W., Camilo, A., Cole, G., Rucker, D., Webster, R. and Fischer, G. (2012). MRI-guided concentric tube continuum robot with piezoelectric actuation: A feasibility study. In *IEEE Int. Conf. Robotics and Automation (ICRA)*, pp. 1939–1945.

65. Eslami, S., Shang, W., Li, G., Patel, N., Fischer, G. S., Tokuda, J., Hata, N., Tempany, C. M. and Iordachita, I. (2015). In-bore prostate transperineal interventions with an MRI-guided parallel manipulator: system development and preliminary evaluation. *The Int. J. Med. Robot. Comput. Assisted Surgery*.
66. Muntener, M., Patriciu, A., Petrisor, D., Ursu, D., Song, D. Y. and Stoianovici, D. (2008). Transperineal prostate intervention: robot for fully automated MR imaging–system description and proof of principle in a canine model. *Radiology*, 247(2), 543–549.
67. van den Bosch, M. R., Moman, M. R., van Vulpen, M., Battermann, J. J. Duiveman, E., van Schelven L. J., de Leeuw, H., Lagendijk, J. J. W. and Moerland, M. A. (2010). MRI-guided robotic system for transperineal prostate interventions: Proof of principle. *Phys. Med. Biol.*, 55(5), N133.
68. Lagerburg, V., Moerland, M. A., van Vulpen, M. and Lagendijk, J. J. (2006). A new robotic needle insertion method to minimize attendant prostate motion. *Radiotherapy Oncol.*, 80(1), 73–77.
69. Chan, K. G., Fielding, T. and Anvari, M. (2016). An image-guided automated robot for MRI breast biopsy. *The Int. J. Med. Robot. Comput. Assisted Sur.*, 12(3), 461–477.
70. Yang, B., Tan, U., Gullapalli, R., McMillan, A. and Desai, J. (2011). Design and implementation of a pneumatically-actuated robot for breast biopsy under continuous MRI. *IEEE ICRA 2011 International Conference on Robotics and Automation*, Shanghai, China.
71. Li, M., Kapoor, A., Mazilu, D. and Horvath, K. (2011). Pneumatic actuated robotic assistant system for aortic valve replacement under MRI guidance. *IEEE Trans. Biomed. Eng.*, 58(2), 443–451.
72. Zemiti, N., Bricault, I., Fouard, C., Sanchez, B. and Cinquin, P. (2008). Lpr: A CT and MR-compatible puncture robot to enhance accuracy and safety of image-guided interventions. *IEEE/ASME Trans. Mechatron.*, 13(3), 306–315.
73. Wu, F. Y., Torabi, M., Yamada, A., Golden, A., Fischer, G. S., Tuncali, K., Frey, D. D. and Walsh, C. (2013). An MRI coil-mounted multi-probe robotic positioner for cryoablation. In *ASME 2013 International Design Engineering Technical Conferences and Computers and Information in Engineering Conference*, American Society of Mechanical Engineers, pp. V06AT07A012–V06AT07A012.
74. Salimi, A., Ramezanifar, A., Mohammadpour, J., Grigoriadis, K. M. and Tsekos, N. V. (2014). Design and qualification of a parallel robotic platform to assist with beating-heart intracardiac interventions. *J. Mech. Robot.*, 6(2), 021004.
75. Hashizume, M., Yasunaga, T., Tanoue, K., Ieiri, S., Konishi, K., Kishi, K., Nakamoto, H., Ikeda, D., Sakuma, I., Fujie, M. and Dohi, T. (2008). New real-time MR image-guided surgical robotic system for minimally invasive precision surgery. *Int. J. Comput. Assisted Radiol. Sur.*, 2, 317–325.
76. Franco, E., Brujic, D., Rea, M., Gedroyc, W. M. and Ristic, M. (2016). Needle-guiding robot for laser ablation of liver tumors under MRI guidance. *IEEE/ASME Trans. Mechatron.*, 21(2), 931–944.
77. Franco, E., Ristic, M., Rea, M. and Gedroyc, W. M. (2016). Robot-assistant for MRI-guided liver ablation: A pilot study. *Med. Phys.*, 43(10), 5347–5356.
78. Krieger, A., Iordachita, I., Song, S.-E., Cho, N., Guion, P., Fichtinger, G. and Whitcomb, L. (2010). Development and preliminary evaluation of an actuated MRI-compatible robotic device for MRI-guided prostate intervention, In *IEEE Int. Conf. Robotics and Automation*, pp. 1066–1073.